

## Coarsening dynamics in the Swift-Hohenberg equation with an external field

Ashwani K. Tripathi,<sup>1,2</sup> Deepak Kumar,<sup>1,\*</sup> and Sanjay Puri<sup>1</sup>

<sup>1</sup>*School of Physical Sciences, Jawaharlal Nehru University, New Delhi – 110067, India*

<sup>2</sup>*Center for Soft and Living Matter, Institute for Basic Science, Ulsan 44919, Republic of Korea*



(Received 24 October 2018; published 26 February 2019)

We study the Swift–Hohenberg equation (SHE) in the presence of an external field. The application of the field leads to a phase diagram with three phases, i.e., stripe, hexagon, and uniform. We focus on coarsening after a quench from the uniform to stripe or hexagon regions. For stripe patterns, we find that the length scale associated with the order-parameter structure factor has the same growth exponent ( $\simeq 1/4$ ) as for the SHE with zero field. The growth process is slower in the case of hexagonal patterns, with the effective growth exponent varying between  $1/6$  and  $1/9$ , depending on the quench parameters. For deep quenches in the hexagonal phase, the growth process stops at late stages when defect boundaries become pinned.

DOI: [10.1103/PhysRevE.99.022136](https://doi.org/10.1103/PhysRevE.99.022136)

### I. INTRODUCTION

This paper studies coarsening dynamics in the Swift–Hohenberg equation (SHE) in the presence of an external field. The SHE has been used extensively as a prototype model to study spatially periodic patterns [1]. The model generates simple stripe patterns and is useful to illustrate several basic and universal features of pattern formation [2–4]. It is derived from a Lyapunov or free-energy functional and leads to stable static patterns.

In the presence of a uniform field, the SHE assumes the following form:

$$\frac{\partial \psi(\vec{r}, t)}{\partial t} = [\epsilon - (\nabla^2 + 1)^2] \psi - \psi^3 + h, \quad (1)$$

where  $\psi(\vec{r}, t)$  is the (real-valued) order-parameter field which depends on space  $\vec{r}$  and time  $t$ . This model has two parameters,  $\epsilon$  and  $h$ , and we study its phase diagram in  $(\epsilon, h)$  space. The field  $h$  breaks the inversion symmetry ( $\psi \rightarrow -\psi$ ) of the SHE. It thus allows for hexagonal patterns which lack parity symmetry. The overall phase diagram is richer and has three patterns: stripe, hexagonal, and uniform. Similar phase diagrams have been studied by introducing other parity-breaking terms [2,5,6], but we find that the introduction of  $h$  provides a simpler physical picture.

Our study is closely related to a physical situation of great interest. Stripe patterns occur in thin magnetic films with strong uniaxial anisotropy normal to the film [7–10]. They result from a competition between long-ranged dipolar interactions and short-ranged exchange interactions. When a strong field is applied perpendicular to the plane of the film, the stripe pattern changes to a hexagonal pattern of bubble domains. These bubble domains have been extensively explored for their potential in information storage [7,8]. Theoretically, this problem was first analyzed by Garel and Doniach [11]. It has also been pursued in several recent studies [10,12–16]. Some recent experiments using Lorentz transmission elec-

tron microscopy have also revealed exotic helicity structures within the domain walls of bubbles [17].

The phase diagram of the  $d = 2$  SHE with a field (see Fig. 1) is very similar to that of a magnetic film in a field [11,18,19]. Thus, we use the SHE to study the diverse patterns (and their dynamics) seen in magnetic films. More generally, stripe and hexagonal morphologies are ubiquitous in the physical world. Thus, our study has rather general applicability.

The subject of growth dynamics of patterns has a long history [20,21]. For the SHE, there have been several studies which have revealed interesting peculiarities associated with the coarsening of equilibrium states with nontrivial spatial structure [6,22–31]. This is natural as the order in these systems requires specification of more properties, and the order-parameter manifold is more complex [32]. For stripes in two dimensions, we need to specify (a) the amplitude of order; and (b) two angles, one denoting the orientation of the normal to stripes and the other its phase of modulations. Furthermore, one needs to study not only the correlations of  $\psi(\vec{r}, t)$ , but also the orientational correlations associated with  $\vec{\nabla} \psi(\vec{r}, t)$ . The latter may exist even when the full order, which is composed of both phase and orientation, is absent [33].

In phase transitions involving uniform states, the growth of the ordered phase obeys *dynamical scaling* [20,21]. More precisely, the correlator of the order-parameter field  $\psi(\vec{r}, t)$  obeys the property

$$\begin{aligned} C_\psi(\vec{r}, t) &= \langle \psi(\vec{R}, t) \psi(\vec{R} + \vec{r}, t) \rangle - \langle \psi(\vec{R}, t) \rangle \langle \psi(\vec{R} + \vec{r}, t) \rangle \\ &= f[r/L(t)]. \end{aligned} \quad (2)$$

Here, the angular brackets denote an average over a nonequilibrium ensemble. The quantity  $L(t)$  is a growing length scale, which is a measure of the size of ordered domains. The length scale grows at large times as a power law,  $L(t) \sim t^\phi$ , where  $\phi$  is the growth exponent.

For stripe patterns studied by using the SHE, similar scaling has been established—for full order as well as orientational order. But two exceptional points have emerged from the past studies [22–28,31]:

\*Deceased.

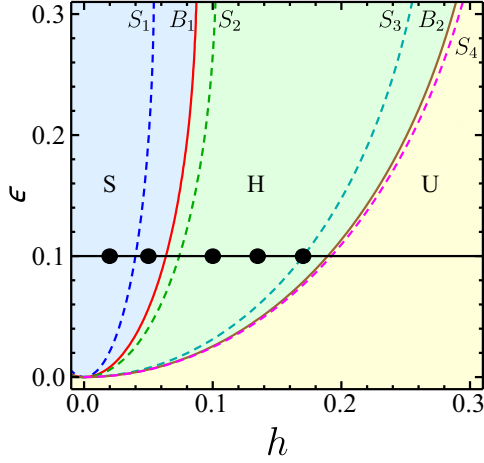


FIG. 1. Phase diagram of Eq. (1) in dimensions  $d = 2$ . Here S, H, U denote the stripe, hexagonal, and uniform phase, respectively.  $S_1$  ( $\epsilon = 51\bar{\psi}^2$ ) and  $S_2$  ( $\epsilon = 15\bar{\psi}^2$ ) are the spinodal boundaries between stripes and hexagons.  $S_3$  ( $\epsilon = 3\bar{\psi}^2$ ) and  $S_4$  ( $\epsilon = 12\bar{\psi}^2/5$ ) are the spinodal boundaries between hexagonal and uniform phases. [Recall that  $\bar{\psi}$  is a function of  $h$  obtained from Eq. (5).]  $B_1[\epsilon = \bar{\psi}^2(3 + 12/[6^{3/2} - 14])]$  is the boundary where stripes and hexagons have the same free energy.  $B_2[\epsilon = 37\bar{\psi}^2/15]$  corresponds to the boundary where hexagons and uniform phases have the same free energy. The black circles show the parameter values studied in our simulations.

(a) Orientational correlations grow faster than those of full order because orientations are not affected by certain kinds of defects. For example, dislocations affect the stripe order but do not disturb the orientational order [33].

(b) The growth slows down as  $\epsilon$  increases, which can largely be attributed to the pinning potential provided by stripes on the larger-scale defect structures [26,31,34–36].

Coarsening in hexagonal patterns has been explored through experimental and numerical studies on block copolymer systems [37–40]. Again, the length-scale associated with orientation correlations grows faster than other correlation lengths [38]. However, the dynamics is very slow compared with the stripe patterns. In some cases, coarsening freezes due to pinning effects [40,41].

The goal of the present paper is to study the coarsening process for different field values. With variation in  $h$ , one moves across the phase diagram which leads to changes in phase as well as the nature of dominant defects. These defects, which depend on the order-parameter manifold, determine the growth exponents in a crucial way. Our main results address the coarsening of stripes and hexagonal patterns in the region of the phase diagram where they are equilibrium phases.

This paper is organized as follows: We discuss the phase diagram of the SHE in Sec. II. In Sec. III, we provide the details of our computational methods. The coarsening dynamics of the stripe phase is discussed in Sec. IV. We present a detailed discussion of the ordering dynamics of hexagonal patterns in Sec. V. Finally, we conclude our paper in Sec. VI.

## II. PHASE DIAGRAM

We want to understand the various phases obtained in the SHE and transitions between them. Therefore, we have obtained the phase diagram for the model using the standard amplitude equation analysis [42–44], which is valid for small values of  $\epsilon$  and  $h$ . Since all the states generated by this model are spatial modulations around a constant amplitude induced by the field, it is useful to write the  $\psi$  field as

$$\psi(\vec{r}, t) = \bar{\psi}(h) + \Phi(\vec{r}, t). \quad (3)$$

Here,  $\bar{\psi}$  is an  $h$ -dependent constant and  $\Phi(\vec{r}, t)$  is the spatial modulation around it. Substituting this into Eq. (1), we obtain

$$\frac{\partial \Phi(\vec{r}, t)}{\partial t} = [(\epsilon - 3\bar{\psi}^2) - (\nabla^2 + 1)^2]\Phi - 3\bar{\psi}\Phi^2 - \Phi^3. \quad (4)$$

The constant  $\bar{\psi}$  is determined by the cubic equation

$$\bar{\psi}^3 - (\epsilon - 1)\bar{\psi} - h = 0. \quad (5)$$

Equation (4) is similar to the SHE except for an additional quadratic term. This term breaks the inversion symmetry of the field  $\Phi$  and therefore allows hexagonal patterns in addition to stripes. The hexagonal order is locally characterized as

$$\Phi_H(\vec{r}, t) = A_1 e^{i\vec{q}_1 \cdot \vec{r}} + A_2 e^{i\vec{q}_2 \cdot \vec{r}} + A_3 e^{i\vec{q}_3 \cdot \vec{r}} + \text{c.c.}, \quad (6)$$

where  $A_1, A_2$ , and  $A_3$  are the amplitudes of the three modes  $\vec{q}_1, \vec{q}_2$ , and  $\vec{q}_3$ . The modes  $\vec{q}_1, \vec{q}_2$ , and  $\vec{q}_3$  denote unit vectors with each vector making an angle  $2\pi/3$  with the other two. The amplitudes in Eq. (6) are complex in general, and c.c. denotes the complex conjugate of the terms in the expression.

The amplitude equation analysis [42–44] is employed on Eq. (4) to yield spacetime evolution equations for the three amplitudes  $A_1, A_2$ , and  $A_3$ . For deriving the phase diagram, the spatial dependence of the amplitudes is not required. Ignoring spatial variations, the amplitude equations are

$$\begin{aligned} \frac{dA_1}{dt} &= \bar{\epsilon}A_1 + \gamma A_2^* A_3^* - g_0[|A_1|^2 + G(|A_2|^2 + |A_3|^2)]A_1, \\ \frac{dA_2}{dt} &= \bar{\epsilon}A_2 + \gamma A_3^* A_1^* - g_0[|A_2|^2 + G(|A_3|^2 + |A_1|^2)]A_2, \\ \frac{dA_3}{dt} &= \bar{\epsilon}A_3 + \gamma A_1^* A_2^* - g_0[|A_3|^2 + G(|A_1|^2 + |A_2|^2)]A_3. \end{aligned} \quad (7)$$

The various parameters in Eq. (7) are

$$\bar{\epsilon} = \epsilon - 3\bar{\psi}^2, \quad \gamma = -6\bar{\psi}, \quad g_0 = 3, \quad G = 2. \quad (8)$$

We can make Eqs. (7) dimensionless by rescaling the amplitudes and time as follows:

$$A_i = \frac{\gamma}{g_0} \tilde{A}_i, \quad i = 1, 2, 3, \quad t = \frac{g_0}{\gamma^2} \tilde{t}. \quad (9)$$

This results in the following equations for the scaled amplitudes:

$$\begin{aligned} \frac{dA_1}{dt} &= \tilde{\epsilon}A_1 + A_2^* A_3^* - [ |A_1|^2 + G(|A_2|^2 + |A_3|^2) ] A_1, \\ \frac{dA_2}{dt} &= \tilde{\epsilon}A_2 + A_3^* A_1^* - [ |A_2|^2 + G(|A_3|^2 + |A_1|^2) ] A_2, \\ \frac{dA_3}{dt} &= \tilde{\epsilon}A_3 + A_1^* A_2^* - [ |A_3|^2 + G(|A_1|^2 + |A_2|^2) ] A_3, \end{aligned} \quad (10)$$

where  $\tilde{\epsilon} = \bar{\epsilon}g_0/\gamma^2$ . For simpler notation, we have dropped the tilde on the amplitudes and time.

It is known that Eqs. (10) admit three classes of static solutions [2,42,43].

(a) *Uniform*:  $A_i = 0$ ,  $i = 1, 2, 3$ .

(b) *Stripes*:  $A_1 = a_S e^{i\phi}$ ,  $A_2 = 0$ ,  $A_3 = 0$ , where  $a_S = \sqrt{\tilde{\epsilon}}$  is the stripe amplitude and  $\phi$  is the phase of the stripe modulation. The phase  $\phi$  is an arbitrary constant and we set it to zero, without any loss of generality.

(c) *Hexagons*:  $A_i = a_H e^{i\phi_i}$ ,  $i = 1, 2, 3$ . There are two types of stationary solutions corresponding to the following conditions on the phases:

(1)  $\phi_1 + \phi_2 + \phi_3 = 0$ . We obtain the following expressions for the amplitude:

$$a_H = \frac{1 \pm \sqrt{1 + 4\tilde{\epsilon}(1 + 2G)}}{2(1 + 2G)}. \quad (11)$$

The solution with the + sign exists for  $\tilde{\epsilon} \geq -1/[4(1 + 2G)]$ , whereas the solution with the - sign exists for  $-1/[4(1 + 2G)] \leq \tilde{\epsilon} \leq 0$ .

(2)  $\phi_1 + \phi_2 + \phi_3 = \pi$ . In this case,

$$a_H = \frac{-1 \pm \sqrt{1 + 4\tilde{\epsilon}(1 + 2G)}}{2(1 + 2G)}. \quad (12)$$

Here, the only acceptable solution is the one with the + sign and exists for  $\tilde{\epsilon} \geq 0$ .

To plot the phase diagram, we study the linear stability of these solutions as a function of  $\tilde{\epsilon}$  in Eqs. (10). This analysis is available in the literature [2,4,5]. When these results are translated to parameters  $\epsilon$  and  $h$ , using Eqs. (8) and  $\tilde{\epsilon} = \bar{\epsilon}g_0/\gamma^2$ , one obtains the phase diagram shown in Fig. 1.

In Fig. 1, the stripe (S) phase is linearly stable in the region between the  $y$  axis ( $h = 0$ ) and the spinodal curve  $S_2$ . Between  $S_2$  and  $S_3$ , stripes are unstable and they cease to exist after  $S_3$ . The hexagonal (H) phase is linearly stable between the spinodal boundaries  $S_1$  and  $S_4$ , and it does not exist to the right of  $S_4$ . The uniform (U) phase exists for all parameters. However, it is linearly stable only above the  $S_3$  boundary. Clearly, the linear stability regions are overlapping. In the region between  $S_1$  and  $S_2$ , both stripes and hexagons are linearly stable. Similarly, in the region between  $S_3$  and  $S_4$ , the hexagonal and uniform phases are linearly stable. This situation is resolved by computing the free energy, because the equilibrium phase is the one with lower free energy.

To calculate the free energy within the amplitude equation framework, we note that Eqs. (10) have potential dynamics given by the free energy

$$\mathcal{F} = \sum_{i=1}^3 \left( -\tilde{\epsilon}|A_i|^2 + \frac{1}{2}|A_i|^4 + \frac{G}{2} \sum_{j=1, j \neq i}^3 |A_i|^2 |A_j|^2 \right) - (\gamma A_1 A_2 A_3 + \text{c.c.}). \quad (13)$$

By using the static solutions given above, the free energies of the three states are easily computed. The curve  $B_1$  is the boundary on which stripe and hexagonal phases have equal free energy. On the left of this curve, stripes have lower free energy, whereas hexagons have lower free energy on the right of  $B_1$ . Similarly, we compare the free energies of hexagonal

and uniform phases and obtain the curve  $B_2$  as the hexagonal-uniform phase boundary.

To summarize Fig. 1, the stripe phase is stable between the  $\epsilon$  axis and  $B_1$  (light-blue region), and it is metastable between  $B_1$  and  $S_2$ . Similarly, the hexagonal phase is stable between  $B_1$  and  $B_2$  (light-green region), and metastable between  $S_1$ - $B_1$  and  $B_2$ - $S_4$ . Finally, the uniform phase is stable to the right of  $B_2$  (light-yellow region), and metastable between  $S_3$ - $B_2$ .

### III. COMPUTATIONAL METHOD

We have used a pseudospectral method to solve Eq. (1) [45,46] in  $d = 2$ . (We impose periodic boundary conditions in both directions.) For this purpose, we rewrite Eq. (1) as

$$\partial_t \psi = \mathcal{L}[\psi] + \mathcal{N}[\psi], \quad (14)$$

where  $\mathcal{L}[\psi]$  and  $\mathcal{N}[\psi]$  represent the ‘‘linear’’ and ‘‘nonlinear’’ parts:

$$\begin{aligned} \mathcal{L}[\psi] &= -(\nabla^2 + 1)^2 \psi, \\ \mathcal{N}[\psi] &= \epsilon \psi - \psi^3 + h. \end{aligned} \quad (15)$$

In principle, one can include the  $\epsilon \psi$  term in the linear part. However, our simulations show that including this term in the nonlinear part leads to a numerical scheme which is stable for a much larger time step ( $\Delta t = 1.0$ ).

We take the Fourier transform of Eq. (14), which gives the following equation for a given mode  $q$  in Fourier space:

$$\partial_t \psi(q, t) = \mathcal{L}(q) \psi(q, t) + \mathcal{N}[\psi(q, t)]. \quad (16)$$

Here,  $\mathcal{L}(q)$  is the eigenvalue of the linear operator for a mode  $q$ . We work in Fourier space and update  $\psi(q, t)$  at each time step. We have used the implicit Euler method [47]. In this method, the linear part is calculated at the advanced time step  $t + \Delta t$ , whereas the nonlinear part is calculated at time  $t$ . This results in the following iterative scheme for Eq. (16):

$$\psi(q, t + \Delta t) = \frac{\psi(q, t) + \Delta t \mathcal{N}[\psi(q, t)]}{1 - \mathcal{L}(q) \Delta t}. \quad (17)$$

Simulations were performed for three different system sizes, viz.,  $N^2$  with  $N = 512, 1024, 2048$ . The lattice spacing and time step are taken to be  $\Delta x = \pi/4$  and  $\Delta t = 1.0$ , respectively. Smaller values of  $\Delta t$  also lead to the same results. The Fourier transforms were calculated via the fast Fourier transform technique using the FFTW3 package [48]. All the simulations were carried out for  $\epsilon = 0.1$ , starting from a uniform random initial condition with  $\psi \in [-0.1, 0.1]$ . We considered five different values of  $h$ . The  $(\epsilon, h)$  values for our simulations are shown by black circles in Fig. 1. All statistical data presented here were obtained as an average over  $N_r$  independent runs. The number of runs for different lattice sizes was  $N_r = 200$  ( $N = 512$ ),  $N_r = 100$  ( $N = 1024$ ), and  $N_r = 50$  ( $N = 2048$ ).

### IV. COARSENING OF STRIPES

We first present results for the coarsening of stripes. This has been earlier studied for the  $h = 0$  case. Coarsening exponents in the range  $1/3$  to  $1/5$  have been reported for the order-parameter structure factor [22,25,28,31], depending

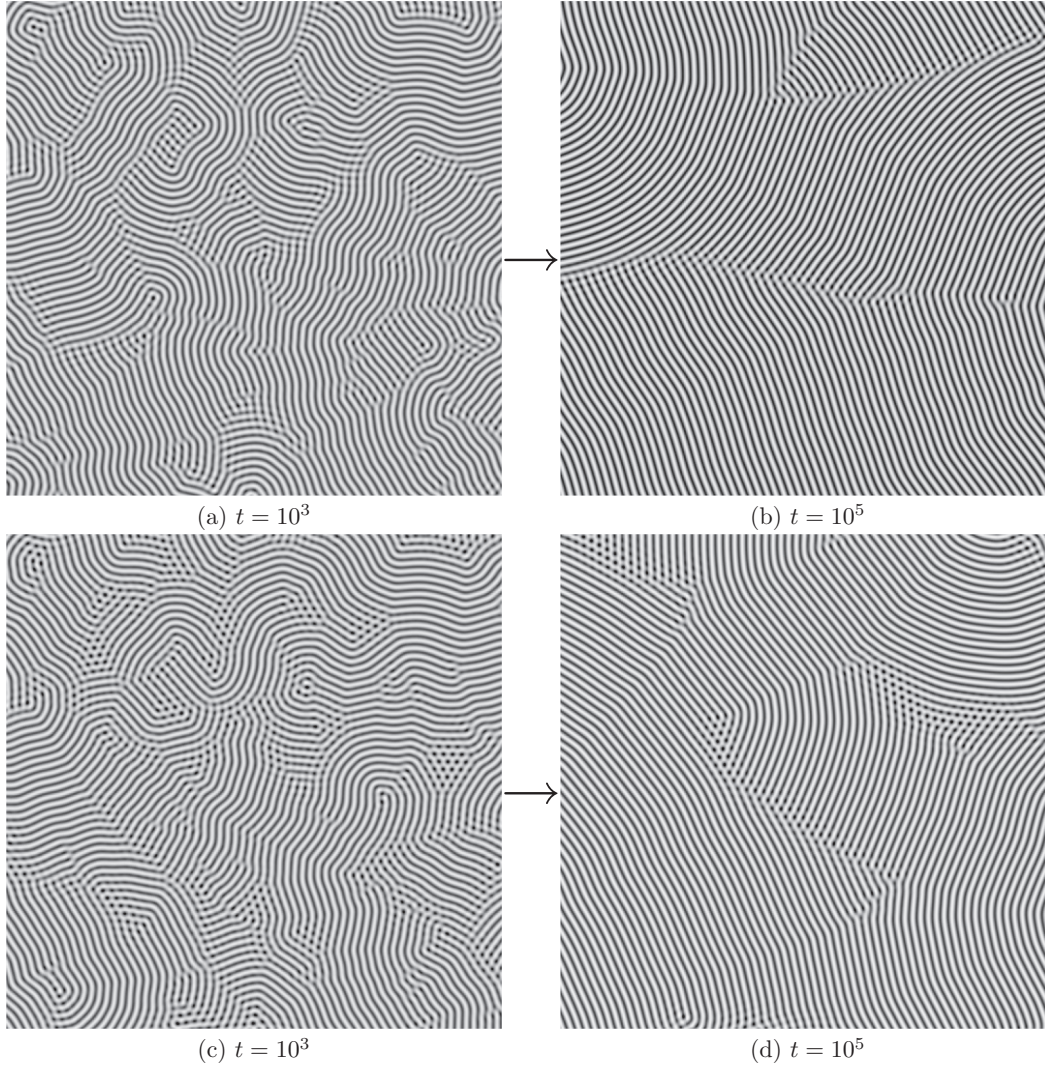


FIG. 2. Evolution of the order parameter  $\psi$  for stripes starting from a random initial state. The snapshots show a  $512^2$  portion carved out from the center of a  $1024^2$  lattice. The top and bottom rows show the evolution for  $h = 0.02$  and  $h = 0.05$ , respectively (see Fig. 1).

on the quench depth  $\epsilon$ . The effective exponent decreases with increase in the quench depth, which is closely related to the type of defects which characterize the coarsening process [28,31]. The defects observed in stripe patterns are isolated defects (disclinations, dislocations) and grain boundaries. These have been observed in experiments on anisotropic magnetic films [7–10]. Dislocations break long-range translational order, whereas disclinations and grain boundaries destroy orientational order [33].

Our simulations of stripe coarsening were primarily performed for  $\epsilon = 0.1$ , and for three different field values:  $h = 0.0, 0.02, 0.05$  (see Fig. 1). For  $h = 0.0$  and  $0.02$ , stripes are the only stable phase. As shown in Figs. 2(a) and 2(b), stripe order grows through annihilation of defects such as grain boundaries, dislocations, and disclinations.

We obtain a qualitatively different evolution for  $h = 0.05$  [see Figs. 2(c) and 2(d)]. For this value of the field, stripes are stable whereas hexagons are metastable. A typical evolution shows that stripe domains are separated by grain boundaries made of hexagonal spots with very few topological defects. The spotted patterns result from the linear superposition of

two or more stripe modes. However, as we see later, this only has a small effect on the growth of the length scale.

For purposes of comparison, we have also considered a shallower quench with  $\epsilon = 0.05$  and  $h = 0.0$ . In an earlier study [31], we investigated the role of defects in the stripe coarsening process at  $h = 0.0$  by varying the quench depth  $\epsilon$ . We showed that, for small  $\epsilon$ , most of the defect regions consist of grain boundaries with a low density of isolated defects such as dislocations and disclinations. By increasing  $\epsilon$ , we observed that the density of grain boundaries decreases whereas the density of isolated defects increases.

We analyze the patterns through the computation of the order-parameter structure factor. This gives us a quantitative measure of the coarsening process through the determination of a length scale over which the patterns are coherent. The structure factor is defined as the Fourier transform of the correlation function:

$$S_\psi(\vec{q}, t) = \int d\vec{r} e^{i\vec{q}\cdot\vec{r}} C_\psi(\vec{r}, t), \quad (18)$$

where  $C_\psi(\vec{r}, t)$  is defined in the first line of Eq. (2). As the patterns are isotropic, we spherically average the vector function  $S_\psi(\vec{q}, t)$  to obtain the scalar function  $S_\psi(q, t)$ , which we show subsequently. The structure factor  $S_\psi(q, t)$  has two dominant peaks: (a) at  $q = 1.0$  (in our dimensionless units), which is the basic periodicity of patterns, and (b) at  $q = 0$ , which is due to the uniform background  $\bar{\psi}$  present when  $h \neq 0$ . The relative strength of these peaks depends on the value of  $h$ .

Let us discuss the evolution of  $S_\psi$  near  $q = 1.0$ . As shown in Fig. 3(a), the peak of the structure factor increases with time, whereas its width decreases. This implies growth of stripe order. To quantify the coarsening, we have fit the data to a square Lorentzian fit [6,23,24]:

$$S_\psi(q, t) = \frac{a^2}{[(q^2 - b)^2 + c^2]}. \quad (19)$$

Then, the full width at half maximum ( $\delta q$ ) is defined as

$$\delta q = \frac{0.322c}{\sqrt{b}}. \quad (20)$$

Here,  $q = \sqrt{b}$  corresponds to the peak of the structure factor. The fitting of the structure factor data shows that it has a peak at  $b = 1$ .

The domain scale is determined as  $L_\psi(t) = 2\pi/\delta q$ . Its time evolution (for a  $2048^2$  lattice) is shown in Fig. 3(b) on a log-log scale. The data for  $\epsilon = 0.1$  and  $h = 0.0, 0.02, 0.05$  shows an excellent power-law behavior for three decades up to  $t = 10^6$ . A line of slope  $1/4$  on the log-log scale, parallel to all three data sets, confirms that the growth exponents are approximately  $1/4$ , which is in accordance with earlier studies [22,25,28,31]. The growth is somewhat faster for the shallower quench with  $\epsilon = 0.05$  and  $h = 0.0$ .

We have also calculated the local coarsening exponent, defined as

$$\phi(t) = \frac{d(\ln L)}{d(\ln t)} = \frac{t}{L} \frac{dL}{dt}. \quad (21)$$

To calculate  $\phi(t)$ , we have used the central-difference formula

$$\frac{dL}{dt} \simeq \frac{L(t + \Delta t) - L(t - \Delta t)}{\Delta t}. \quad (22)$$

We estimate the statistical error in  $\phi(t)$  from the corresponding error in determining  $L(t)$ . Using this, we find that the maximum relative error in the estimation of  $\phi(t)$  is less than 4%. The variation of  $\phi(t)$  with  $t$  is shown in Fig. 3(c).

A closer look at the  $L_\psi$  data [see Fig. 3(b)] suggests that  $L_\psi$  decreases slightly with increase in the external field when  $\epsilon = 0.1$ . This decrease is more prominent for  $h = 0.05$ . We believe that this is related to the presence of hexagonal spots in the defect regions [see Figs. 2(c) and 2(d)], which annihilate slower than other defects. This slower growth also reflects in the variation of the local exponent  $\phi(t)$ , which remains smaller than  $1/4$  for more time than for  $h = 0.0, 0.02$  [see Fig. 3(c)]. We also calculate the average exponent  $\phi_{av}$  by averaging  $\phi(t)$  over time, ignoring the initial transients. We obtain  $\phi_{av} = 0.276$  ( $h = 0.0$ ),  $0.256$  ( $h = 0.02$ ), and  $0.237$  ( $h = 0.05$ ). Thus, the average exponent also confirms the slowing down of growth with increase in  $h$ .

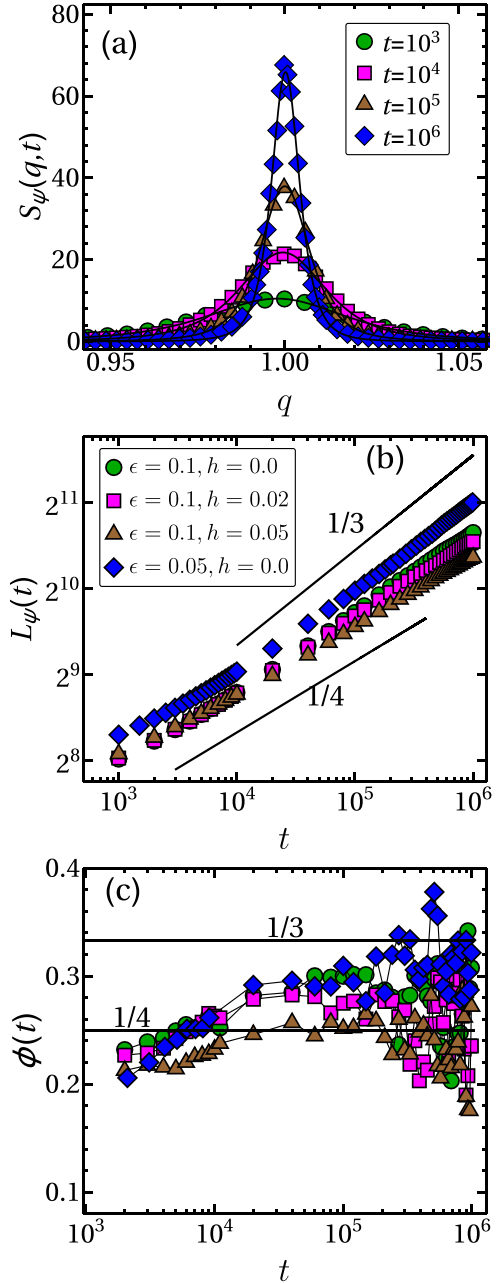


FIG. 3. Evolution of (a) Structure factor  $S_\psi(q, t)$  for  $\epsilon = 0.1$ ,  $h = 0.05$ . (b) Length scale  $L_\psi(t)$  for  $\epsilon = 0.1$ ,  $h = 0.0, 0.02, 0.05$ , and  $\epsilon = 0.05$ ,  $h = 0.0$ , on a log-log scale. (c) Local exponent  $\phi(t)$  for the length-scale data on a log-linear scale. The data sets are obtained on  $2048^2$  lattices. The black lines in panel (a) represent the best fit to the structure factor data by the square Lorentzian in Eq. (19). The black lines in panel (b) denote power laws with exponents  $1/4$  and  $1/3$ . The black lines in panel (c) correspond to the coarsening exponents  $1/4$  and  $1/3$ . The symbols in panel (c) have the same meaning as those in panel (b).

As mentioned earlier, we also performed another simulation for  $\epsilon = 0.05$  and  $h = 0.0$ . As shown in Fig. 3(b), the average domain size exhibits a power-law growth similar to the above study. However, the growth exponent is closer to  $1/3$ , as compared with  $1/4$  for  $\epsilon = 0.1$ . This is consistent with earlier studies [26,27,31], as the dynamics in this case is

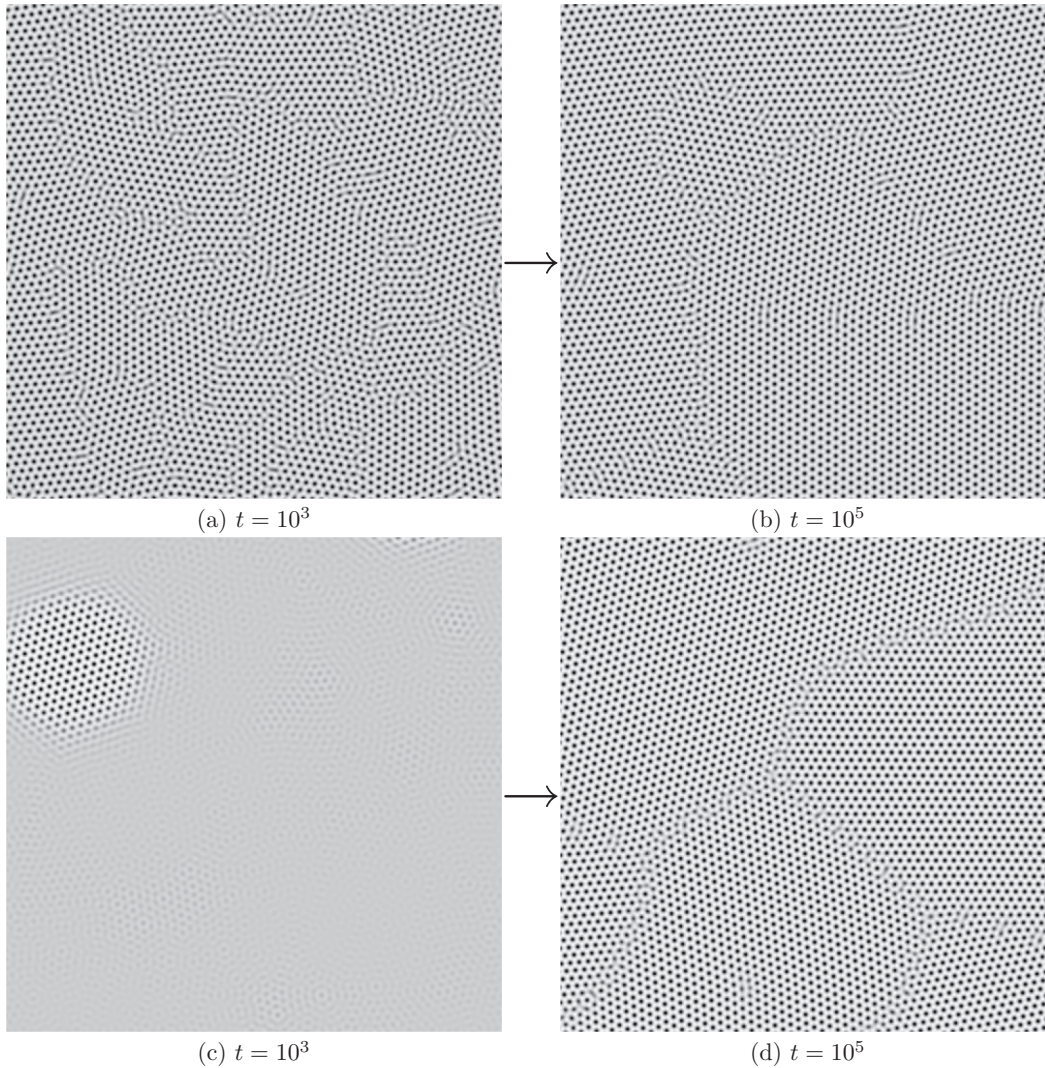


FIG. 4. Evolution of hexagonal patterns starting from a random initial condition. Each snapshot corresponds to a portion of size  $512^2$  carved out from the center of a  $2048^2$  lattice. The top and bottom rows correspond to  $h = 0.1$  and  $0.17$ , respectively (see Fig. 1).

dominated by the evolution of grain boundaries. This is also confirmed by the average value of the local exponent  $\phi(t)$  over time, which is  $\phi_{\text{av}} = 0.31$ .

### V. COARSENING OF HEXAGONS

We next focus on the coarsening of hexagonal patterns. We again fixed  $\epsilon = 0.1$ , and considered three field values,  $h = 0.1, 0.135, 0.17$  (see Fig. 1). We performed simulations for three different lattice sizes, the biggest being  $N = 2048$ . To the best of our knowledge, this is the largest system size used to study the coarsening dynamics of hexagonal patterns. As we will see shortly, it allows us to investigate the kinetics up to  $t = 10^6$  without the occurrence of finite-size effects. For the first two values of the field, only hexagons are the stable phase. The third value lies on the boundary  $S_3$ , where hexagons are stable, and the uniform state is marginally stable (see Fig. 1). We will now discuss in detail the evolution of the hexagonal phase for these three field values.

Figures 4(a) and 4(b) show the morphological evolution of hexagonal patterns for  $h = 0.1$ , starting from a random initial condition. Here, fully formed hexagonal domains appear after some transient evolution (typically  $t > 10^2$ ). These domains are separated by grain boundaries made of penta-hepta defect pairs. The growth of domains occurs through the annihilation of these defects. We observe a steady growth of domains until  $t \simeq 10^5$ . After that, the growth starts to slow down and stagnates in a metastable state at very late stages ( $t \simeq 5 \times 10^5$ ). A similar morphological evolution has also been observed for  $h = 0.135$  (not shown here).

Next, we discuss the growth of hexagonal patterns for  $h = 0.17$  [see Figs. 4(c) and 4(d)]. At early times ( $t \simeq 10^3$ ), the evolution is governed by the linear superposition of modes, leading to the nucleation of small hexagonal regions. These grow as hexagonal fronts propagate into the metastable uniform regions [49]. At a later stage, these hexagonal domains coalesce leading to the formation of grain boundaries made of penta-hepta defects. We do not observe any saturation of the growth, and domains grow uniformly until the largest

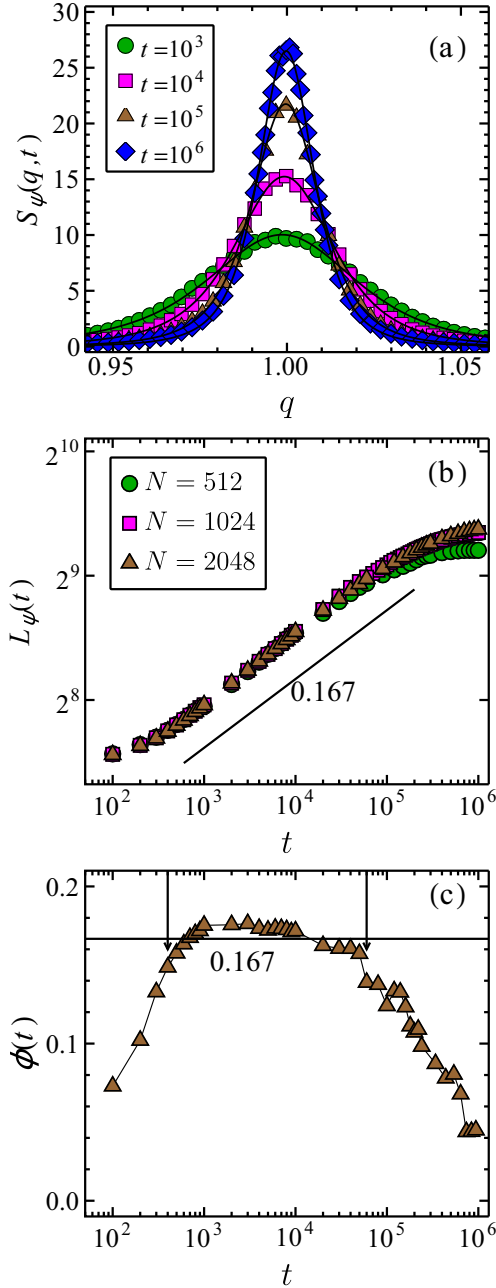


FIG. 5. Domain growth for  $h = 0.1$ , in the hexagonal phase. Evolution of (a) structure factor  $S_\psi(q, t)$ , (b) length scale  $L_\psi$  on a log-log scale, and (c) local exponent  $\phi(t)$  on a log-linear scale. The data in panels (a) and (c) are obtained from  $2048^2$  lattices. The black lines in panel (a) denote the best fit to the structure factor data by the square Lorentzian in Eq. (19). The black line in panel (b) shows a power law with exponent 0.167, which is also marked in panel (c).

time of our simulation,  $t = 10^6$ . However, as we show later, the coarsening exponent is very small in this case ( $\simeq 1/9$ ). As mentioned earlier,  $h = 0.17$  lies on the linear stability boundary  $S_3$  of the uniform phase.

To characterize the coarsening process, we calculate  $S_\psi$  and its associated length scale  $L_\psi(t)$ , defined in Sec. IV. We first present results for  $h = 0.1$ . Figure 5(a) demonstrates the evolution of  $S_\psi$ . The width of  $S_\psi$  becomes narrower, and its

peak gets larger with time, which implies domain coarsening. However, at late stages ( $t > 5 \times 10^5$ ), the coarsening of the peak stops. This is consistent with the morphological evolution shown in Figs. 4(a) and 4(b).

Next, we discuss the behavior of  $L_\psi$ . As shown in Fig. 5(b), we obtain an excellent power-law behavior for  $L_\psi(t)$  over two decades of evolution ( $3 \times 10^2 < t < 6 \times 10^4$ ). The black line parallel to the data shows that the coarsening exponent is consistent with  $\phi \simeq 0.167 = 1/6$ . However,  $L_\psi(t)$  start to slows down after  $t = 10^5$  and saturates at late stages. This is not due to finite-size effects because different lattice sizes ( $N = 1024, 2048$ ) show approximately the same saturation behavior. The system is clearly becoming trapped in a metastable state at late times. We also report the local coarsening exponent  $\phi(t)$ . As shown in Fig. 5(c) corresponding to  $N = 2048$ ,  $\phi(t)$  shows a good agreement with  $\phi = 0.167$  up to  $t = 6 \times 10^4$ .

We present results for  $h = 0.17$  in Fig. 6. In this case, we see a uniform coarsening of  $S_\psi$  over our simulation timescales for the largest system size  $N = 2048$  [see Fig. 6(a)]. This is confirmed by the power-law growth for  $L_\psi$  shown in Fig. 6(b). (Here, the smallest system size of  $N = 512$  shows a coarsening arrest at late times due to finite-size effects.) We obtain an effective growth exponent close to 0.11 ( $\simeq 1/9$ ), smaller than the corresponding exponent at  $h = 0.1$ . A plot of the local exponent  $\phi(t)$  in Fig. 6(c) also confirms the presence of the smaller coarsening exponent over almost three decades. We should emphasize that power laws with small exponents are difficult to distinguish from logarithmic growth laws. We also attempted to fit the  $L_\psi$  vs  $t$  data for  $N = 2048$  by a logarithmic law:  $L_\psi \sim \ln(t/\tau)$ , but this did not yield a reasonable fit. This indicates the absence of logarithmic growth in the time windows considered.

How do we reconcile these different exponents for coarsening in the hexagonal phase? Our intuitive expectation is that the same exponent should apply in a given phase. To understand this, we have to focus on the defects that drive coarsening. For parameter values deep inside the hexagonal phase (Fig. 1), the domain boundaries consist of penta-hepta defects [see Figs. 4(a) and 4(b)]. On the other hand, in the vicinity of phase boundaries, other defects also manifest themselves, e.g., grain boundaries near  $B_1$  and the uniform phase near  $B_2$  [see Figs. 4(c) and 4(d)]. These additional defects populate the domain boundaries, and must be accounted for in any comprehensive understanding of coarsening in the hexagonal phase.

As we have seen in Fig. 5, coarsening via penta-hepta defects is arrested by trapping in metastable states. We understand this saturation in terms of the pinning effects. In the case of crystalline patterns, the underlying periodicity of the patterns offers a potential barrier for the defects [27,34–36,41]. The pinning potential introduces a fixed length scale. Domains get trapped by this potential when the average domain size becomes comparable to this length scale. The pinning potential crucially depends on the quench parameters  $\bar{\epsilon}$  and  $\bar{\psi}$  [41]. For quenches deep in the hexagonal phase, e.g.,  $h = 0.1$  ( $\bar{\epsilon} \simeq 0.064$  and  $\bar{\psi} \simeq 0.11$ ) and  $h = 0.135$  ( $\bar{\epsilon} \simeq 0.04$  and  $\bar{\psi} \simeq 0.15$ ), defects face a large potential barrier. In the absence of sufficient driving force or external fluctuations, the grain boundaries get pinned in metastable states. On the other hand, for  $h = 0.17$  ( $\bar{\epsilon} \simeq 0$  and  $\bar{\psi} \simeq 0.18$ ) in Fig. 6, the pinning

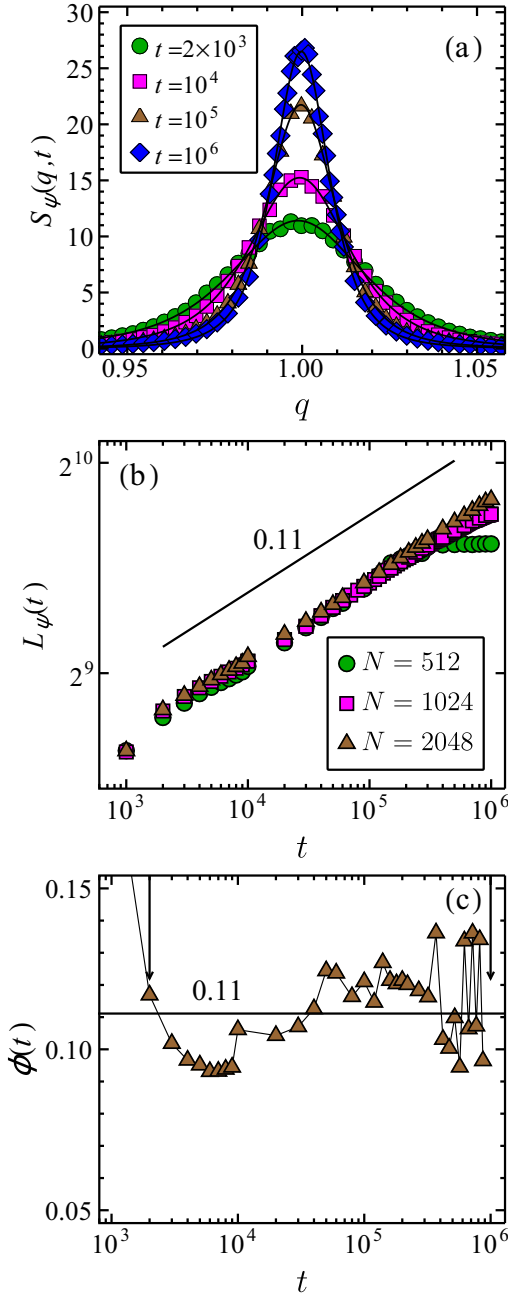


FIG. 6. Domain growth for  $h = 0.17$ , in the hexagonal phase. Evolution of (a) structure factor  $S_\psi(q, t)$ , (b) length scale  $L_\psi(t)$  on a log-log scale, and (c) local exponent  $\phi(t)$  on a log-linear scale. The data in panels (a) and (c) are obtained from  $2048^2$  lattices. The black lines in panel (a) denote the best fit to the square Lorentzian. The black line in panel (b) shows a power law with exponent 0.11, which is also marked in panel (c).

effects are very small. This parameter value lies on the linear stability boundary  $S_3$  of the uniform phase and corresponds to a shallow quench. Here, we observe an uninterrupted growth of domains for the largest times of our simulations.

We have also studied the scaling of the structure factor data according to the following scaling relation [22]:

$$S_\psi(q, t) = L_\psi(t)g[(q-1)L_\psi], \quad (23)$$

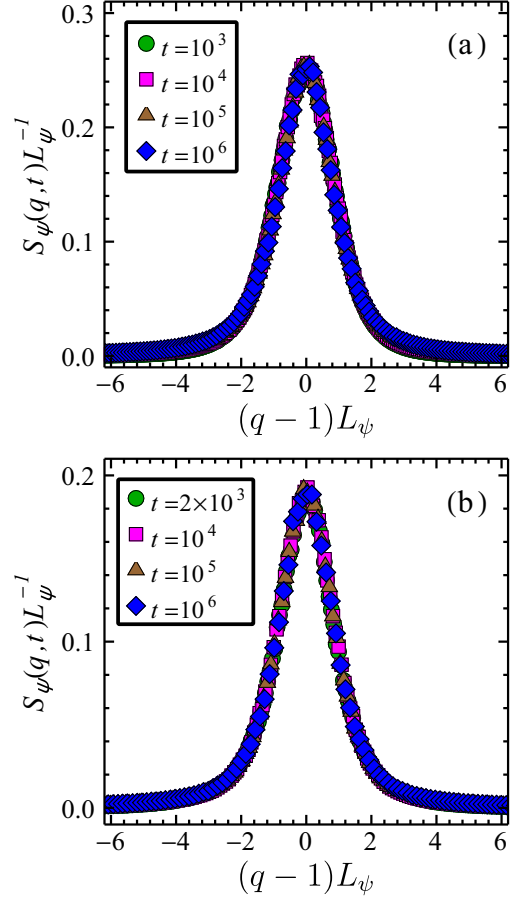


FIG. 7. Scaling of  $S_\psi(q, t)$  for hexagonal patterns in cases with (a)  $h = 0.1$ , and (b)  $h = 0.17$ .

where  $g(x)$  is a universal function of its arguments. Figures 7(a) and 7(b) show the scaling of  $S_\psi$  for  $h = 0.1$  and  $0.17$ , respectively. We obtain an excellent data collapse which confirms the scaling behavior in Eq. (23).

## VI. CONCLUSION

In this paper, we studied coarsening in the Swift–Hohenberg equation (SHE) in the presence of an external field. The external field breaks the inversion symmetry of the order parameter  $\psi$ . This allows the formation of hexagons, in addition to stripe and uniform phases. We have obtained the phase diagram in Fig. 1 from a linear stability analysis of these phases by using an amplitude equation approach. The phase diagram contains two spinodal regimes: one between stripes and hexagons, and another between hexagons and the uniform phase. For quenches deep inside a phase, coarsening is driven by the primary defects associated with that phase. However, for quenches into spinodal regions, we expect secondary defects to also affect the coarsening process.

We have studied domain growth subsequent to a quench from the disordered phase to the stripe and hexagon phases. In the stripe phase, we have considered two parameter values: (a) where the stripe phase is the only stable phase (between  $\epsilon = 0$  and  $S_1$ ), and (b) where the stripe phase is stable, and the hexagonal phase is metastable (between  $S_1$  and  $B_1$ ).

In both cases, we obtain a growth exponent close to  $1/4$ , which is consistent with earlier studies. However, in the latter case, the grain boundaries between two stripe domains also contain hexagonal spots. These annihilate at a slower rate compared with the standard defects associated with stripes. The computation of time-averaged exponents from the local exponent data confirms this behavior.

We have also studied domain growth in regions where hexagons are the equilibrium phases. Again, we have considered parameter values where (a) hexagons constitute the only phase, and (b) a metastable uniform phase may also be present (see Fig. 1). Our study shows that hexagons have much slower growth than stripes with an effective growth exponent ranging between 0.167 and 0.11. We believe that this slow growth is related to penta-hepta defects in the domain boundaries, which annihilate much slower than dislocations and disclinations in stripe patterns. The presence of a metastable uniform phase in the domain boundaries can further complicate the growth scenario. For the deep quenches ( $h = 0.1, 0.135$ ), the growth started to slow down after  $t = 10^5$ , and even stops at late stages. This occurs because the underlying periodicity of the patterns offers a potential barrier for the defects. In the absence of the sufficient driving force to overcome this barrier, defects remain pinned, which stagnates the growth [41]. Thermal fluctuations may activate the motion of the defects by overcoming this barrier to resume the growth process [37,38,40].

Before concluding, it is important to summarize some experimental results in this context. Block copolymers are perhaps the most studied experimental systems for the coarsening of stripes [50–54] and hexagons [37–40,55]. For stripe patterns, coarsening proceeds through the annihilation of multipoles of disclinations (on a smooth substrate) [50,51], or via the annihilation of dislocations (on a patterned substrate) [53]. Here, the orientational correlation length has been shown to grow as  $t^{1/4}$ . This is consistent with our exponents for the length scale associated with the structure factor. In exper-

imental studies on block copolymer films with hexagonal order, it was shown that most of the defects are condensed in grain boundaries [37,38]. This is also in agreement with our simulations.

Several numerical simulations of block copolymers, using a Cahn–Hilliard model, have also reported that the orientational correlations grow through annihilation of dislocations [38]. In addition, simulations have also shown that triple junctions can slow the dynamics of defect annihilation and lead to the formation of metastable configurations through the pinning of the triple junctions [40,55]. It would clearly be relevant to explore the role of triple junctions in the growth of hexagonal order in our simulations.

In summary, our understanding of stripe coarsening is good but that of hexagon coarsening remains incomplete. At the same time, hexagon coarsening is experimentally very important and arises in myriad physical applications. Therefore, this is clearly an important direction for future studies of domain growth in the SHE. We identify some outstanding issues which need to be addressed in this context:

- (a) the role of metastable phases in modifying effective growth exponents in hexagon ordering;
- (b) the role of grain boundaries and triple junctions in the coarsening of hexagons;
- (c) the role of thermal fluctuations in preventing the trapping of penta-hepta defects in local minima;
- (d) the formulation of an analytic argument for the growth exponent in hexagon coarsening, in analogy with those for coarsening via domain walls [21], and disclinations or dislocations [25].

#### ACKNOWLEDGMENT

A.K.T. gratefully acknowledges financial support from the University Grants Commission, India. S.P. is grateful to the Department of Science and Technology, India, for funding through a J.C. Bose fellowship.

- 
- [1] J. Swift and P. C. Hohenberg, *Phys. Rev. A* **15**, 319 (1977).
  - [2] M. C. Cross and H. Greenside, *Pattern Formation and Dynamics in Nonequilibrium Systems* (Cambridge University Press, Cambridge, 2009).
  - [3] R. Hoyle, *Pattern Formation: An Introduction to Methods* (Cambridge University Press, Cambridge, 2006).
  - [4] M. C. Cross and P. C. Hohenberg, *Rev. Mod. Phys.* **65**, 851 (1994).
  - [5] S. Ciliberto, P. Coulet, J. Lega, E. Pampaloni, and C. Perez-Garcia, *Phys. Rev. Lett.* **65**, 2370 (1990).
  - [6] H. Ohnogi and Y. Shiwa, *Phys. Rev. E* **84**, 011611 (2011).
  - [7] A. P. Malozemoff and J. C. Slonczewski, *Magnetic Domain Walls in Bubble Materials* (Academic Press, New York, 1979).
  - [8] A. Hubert and R. Schäfer, *Magnetic Domains* (Springer, Berlin, 1998), pp. 499–509.
  - [9] M. D. P. Martínez, J. Milano, M. Eddrief, M. Marangolo, and S. Bustingorry, *J. Phys.: Condens. Matter* **28**, 136001 (2016).
  - [10] K. Chesnel, A. S. Westover, C. Richards, B. Newbold, M. Healey, L. Hindman, B. Dodson, K. Cardon, D. Montealegre, J. Metzner, T. Schneider, B. Böhm, F. Samad, L. Fallarino, and O. Hellwig, *Phys. Rev. B* **98**, 224404 (2018).
  - [11] T. Garel and S. Doniach, *Phys. Rev. B* **26**, 325 (1982).
  - [12] A. B. Kashuba and V. L. Pokrovsky, *Phys. Rev. B* **48**, 10335 (1993).
  - [13] E. A. Jagla, *Phys. Rev. E* **70**, 046204 (2004).
  - [14] D. Clarke, O. A. Tretiakov, and O. Tchernyshyov, *Phys. Rev. B* **75**, 174433 (2007).
  - [15] N. Abu-Libdeh and D. Venus, *Phys. Rev. B* **84**, 094428 (2011).
  - [16] T. H. Johansen, A. V. Pan, and Y. M. Galperin, *Phys. Rev. B* **87**, 060402(R) (2013).
  - [17] X. Yu, M. Mostovoy, Y. Tokunaga, W. Zhang, K. Kimoto, Y. Matsui, Y. Kaneko, N. Nagaosa, and Y. Tokura, *Proc. Natl. Acad. Sci. USA* **109**, 8856 (2012).
  - [18] C. Roland and R. C. Desai, *Phys. Rev. B* **42**, 6658 (1990).
  - [19] A. Mendoza-Coto, O. V. Billoni, S. A. Cannas, and D. A. Stariolo, *Phys. Rev. B* **94**, 054404 (2016).
  - [20] A. J. Bray, *Adv. Phys.* **43**, 357 (1994).

- [21] *Kinetics of Phase Transition Dynamics*, edited by S. Puri and V. K. Wadhawan (CRC Press, Florida, 2009).
- [22] K. R. Elder, J. Viñals, and M. Grant, *Phys. Rev. Lett.* **68**, 3024 (1992); *Phys. Rev. A* **46**, 7618 (1992).
- [23] M. C. Cross and D. I. Meiron, *Phys. Rev. Lett.* **75**, 2152 (1995).
- [24] Q. Hou, S. Sasa, and N. Goldenfeld, *Physica A (Amsterdam, Neth.)* **239**, 219 (1997).
- [25] J. J. Christensen and A. J. Bray, *Phys. Rev. E* **58**, 5364 (1998).
- [26] D. Boyer and J. Viñals, *Phys. Rev. E* **64**, 050101(R) (2001).
- [27] D. Boyer and J. Viñals, *Phys. Rev. E* **65**, 046119 (2002).
- [28] H. Qian and G. F. Mazenko, *Phys. Rev. E* **67**, 036102 (2003).
- [29] H. Qian and G. F. Mazenko, *Phys. Rev. E* **69**, 011104 (2004).
- [30] A. K. Tripathi and D. Kumar, *Phys. Rev. E* **90**, 022915 (2014).
- [31] A. K. Tripathi and D. Kumar, *Phys. Rev. E* **91**, 022923 (2015).
- [32] B. G. Chen, G. P. Alexander, and R. D. Kamien, *Proc. Natl. Acad. Sci. USA* **106**, 15577 (2009).
- [33] J. Toner and D. R. Nelson, *Phys. Rev. B* **23**, 316 (1981).
- [34] Y. Pomeau, *Physica D* **23**, 3 (1986).
- [35] D. Bensimon, B. I. Shraiman, and V. Croquette, *Phys. Rev. A* **38**, 5461 (1988).
- [36] B. A. Malomed, A. A. Nepomnyashchy, and M. I. Tribelsky, *Phys. Rev. A* **42**, 7244 (1990).
- [37] C. Harrison, D. E. Angelescu, M. Trawick, Z. Cheng, D. A. Huse, P. M. Chaikin, D. A. Vega, J. M. Sebastian, R. A. Register, and D. H. Adamson, *Europhys. Lett.* **67**, 800 (2004).
- [38] D. A. Vega, C. K. Harrison, D. E. Angelescu, M. L. Trawick, D. A. Huse, P. M. Chaikin, and R. A. Register, *Phys. Rev. E* **71**, 061803 (2005).
- [39] L. R. Gómez, E. M. Vallés, and D. A. Vega, *Phys. Rev. Lett.* **97**, 188302 (2006).
- [40] L. R. Gómez, E. M. Vallés, and D. A. Vega, *Physica A (Amsterdam, Neth.)* **386**, 648 (2007).
- [41] D. Boyer and J. Viñals, *Phys. Rev. Lett.* **89**, 055501 (2002).
- [42] L. A. Segel, *J. Fluid Mech.* **38**, 203 (1969).
- [43] A. C. Newell and J. A. Whitehead, *J. Fluid Mech.* **38**, 279 (1969).
- [44] D. Walgraef, *Spatio-Temporal Pattern Formation: With Examples from Physics, Chemistry, and Materials Science* (Springer-Verlag, New York, 1997).
- [45] C. Canuto, M. Hussaini, A. Quarteroni, and J. A. Thomas, *Spectral Methods in Fluid Dynamics* (Springer, Berlin, 1987).
- [46] M. C. Cross, D. Meiron, and Y. Tu, *Chaos* **4**, 607 (1994).
- [47] W. H. Press, S. A. Teukolsky, W. T. Vetterling, and B. P. Flannery, *Numerical Recipes 3rd Edition: The Art of Scientific Computing* (Cambridge University Press, Cambridge, 2007).
- [48] M. Frigo and S. G. Johnson, *Proc. IEEE* **93**, 216 (2005).
- [49] A. D. Pezzutti, L. R. Gómez, M. A. Villar, and D. A. Vega, *Europhys. Lett.* **87**, 66003 (2009).
- [50] C. Harrison, D. H. Adamson, Z. Cheng, J. M. Sebastian, S. Sethuraman, D. A. Huse, R. A. Register, and P. M. Chaikin, *Science* **290**, 1558 (2000).
- [51] C. Harrison, Z. Cheng, S. Sethuraman, D. A. Huse, P. M. Chaikin, D. A. Vega, J. M. Sebastian, R. A. Register, and D. H. Adamson, *Phys. Rev. E* **66**, 011706 (2002).
- [52] D. A. Vega, L. R. Gómez, A. D. Pezzutti, F. Pardo, P. M. Chaikin, and R. A. Register, *Soft Matter* **9**, 9358 (2013).
- [53] A. D. Pezzutti, L. R. Gómez, and D. A. Vega, *Soft Matter* **11**, 2866 (2015).
- [54] A. A. Abate, G. T. Vu, A. D. Pezzutti, N. A. García, R. L. Davis, F. Schmid, R. A. Register, and D. A. Vega, *Macromolecules (Washington, DC, U. S.)* **49**, 7588 (2016).
- [55] N. A. García, A. D. Pezzutti, R. A. Register, D. A. Vega, and L. R. Gómez, *Soft Matter* **11**, 898 (2015).